Solar Energy Materials & Solar Cells 251 (2023) 112181

Contents lists available at ScienceDirect

Solar Energy Materials and Solar Cells

journal homepage: www.elsevier.com/locate/solmat

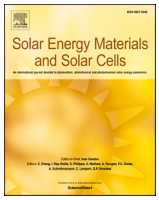

Toward the recovery of solar silicon from end-of-life PVs by vacuum refining

Arman Hoseinpur [a,b,*], Kai Tang [c], Alexander Ulyashin [c], Wolfram Palitzsch [d], Jafar Safarian [a,b]

[a] Department of Materials Science and Engineering, Norwegian University of Science and Technology (NTNU), Norway
[b] Norwegian Center for Sustainable Solar Cell Technology, Norway
[c] SINTEF Industry, Forskningsveien 1, 0314, Oslo, Norway
[d] Lux Chemtech GmbH, Alfred Lange Straße 18, 09599, Freiberg, Germany

ARTICLE INFO

Keywords:
End-of-life Si cells (EoL-Si)
Vacuum refining
Solar-si
Si feedstock
Recovery
Evaporation

ABSTRACT

Considering the boom of Si solar cell installation, it is necessary to establish a process for recycling of Si from End-of-life photovoltaics (PVs). Silicon in the PVs is synthetically doped and coated by various elements and hence dedicated methods will be required for recycling of Si, back to the SoG-Si. In this research, recycling of Si from the shredded solar cells is studied by means of vacuum refining process. In this research the rejected solar cells after the firing step are treated by acid etching techniques to remove the Al back layer and the Ag finger on the front side of the cells, providing a product called de-metallized Si fragments. The vacuum refining experiments were carried out on demetallized Si fragments. Results showed the demetallized Si contained presence of P (11.67 ppmw), B (1 ppmw), Ca with up to 0.28 wt%, Ag (96 ppmw) and Sn (136 ppmw), while other metallic impurities were lower. We have shown that Sn, Ag, O, N, and Mg can be removed from the Si melt via short vacuum refining, while a complete removal of Ca and P required longer times compared to the mentioned impurities. Because vacuum refining process is not limited by thermodynamic equilibrium, a full removal of all the volatile impurities at extended times is expected and then this process has a high chance for returning the recovered Si to the solar grade requirements.

1. Introduction

Photovoltaic (PV) panels are being installed with a high pace and the accumulated installed capacity in the world is just passed 1 TW, which is enough to power the whole Europe [1,2]. Silicon based PV panels comprise a major part of the market (90–95%) and considering a life span of 25–30 years, huge amount of PV wastes is forthcoming. The first wave of EoL-PV panels is expected to be from Japan and Germany [3]. Forecasts stand for 8 million metric tons of PVs ending their life by 2030s and 80 million tons by 2050 [4]. This translates in lots of PV wastes including glass, Si, silver, Al, ethylene vinyl acetate (EVA), etc. [3,5–7]. There are various numbers reported in literature for Si fraction in PV panels, but by considering the lower reported value of 3 wt% [4] and higher reported value of 6.27 wt% [5], we can expect 2.45 to 5 million tons Si. The silicon wafer in the solar cell has received dedicated chemical treatments, to get purified and is also coated and doped by other elements to provide the p-n junction [4]. Considering the conductive tapes, dopped layers, the passivated silicon oxide and/or nitride the EoL-Si contains different impurities than those in the primary Si produced by submerged arc furnaces. Therefore, the EoL-Si should be regarded as a new source for the Si material and new refining techniques should be developed for the recovery of Si. It is worth to mention that in addition to high quality Si recovery, other elements such as Ag and Al should be regarded when dealing with the EoL-Si, and a full recovery of Ag shall be included in the process due to resources shortcoming of silver and its high price. The architecture of a standard c-Si cell is schematically shown in Fig. 1, and clear SEM images can be found in Refs. [8,9]. As shown, these cells are consisted of a silver contact finger on the top surface of Si, the anti-reflex coating (ARC, SiN_x) and the emitter layer, the Si wafer, back surface field layer (BSF), Al–Si layer (eutectic layer), and the porous screen-printed Al back layer.

Various projects [6,10] have been implemented on the recovery of the EoL-PVs and up to now solutions are given for recycling of the glass [11–13], recovery of the silver [14–21], but still there is no scalable method for the recovery of Si from PVs and rebuilding the solar cells. Various techniques and technologies have been applied for the recovery of the materials from c-Si cells and about 178 patents were filed in

* Corresponding author. Department of Materials Science and Engineering, Norwegian University of Science and Technology (NTNU), Norway.
E-mail address: arman.h.kermani@ntnu.no (A. Hoseinpur).

https://doi.org/10.1016/j.solmat.2023.112181
Received 21 September 2022; Received in revised form 4 November 2022; Accepted 2 January 2023

Nomenclature

PVs	Photovoltaics
Demetallized Si	A Si product from c-Si solar cells that is etched by acids for removal of the Ag finger and Al back layer
EoL-PV	end-of-life photovoltaics, standing for the PVs after their service time.
c-Si cells	Crystalline Si solar cells
EoL-Si	The c-Si cell separated from the PV panel
SoG-Si	Solar grade Si, a Si which has a minimum purity of 6 N
PV-Si	A silicon suitable for making c-Si solar cells. This product might have some impurities like P and B, in the level that they can compensate their negative effects
ARC	Anti-reflection coatings
BSF	Back surface field contains a region which is higher doped at the solar cell's rear surface

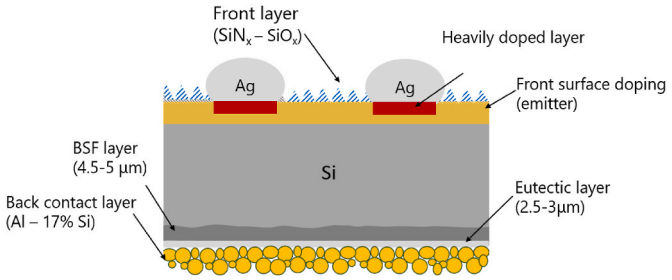

Fig. 1. The schematic representation of a conventional c-Si cell showing the Al back contact layer, eutectic layer, back surface field (BSF), Si wafer, n^+ emitter layer (P doped), SiN_x and SiO_x front layers, and Ag fingers.

between 1976 and 2016 [3]. The most applied methods for the recovery of the elements have been mechanical treatments for crushing the cells and chemical approaches [3]. Acid leaching technique has already found to be useful for the removal of the Al back layer and the Ag contact fingers [10,17–21]. Other approaches like valorization of Si for anode materials applications in the Li-ion batteries [22] and synthesis of silica nano particles [14] has also been studied.

When it comes to recycling of the Si from EoL-PVs, the challenge is dealing with the diffused layers (emitter and BSF layer) as well as the SiO_x - SiN_x coatings. The etching approach does not work for the ARC layer and if etching is applied for the removal the emitter and BSF layers, it leads to considerable Si loss. The vacuum refining process however can fix these challenges and refine the EoL-Si with a lower Si loss. Vacuum refining (VR) of primary Si for removal of its intrinsic impurities, particularly phosphorus (P), has been studied since 1990s [23–26] leading to promising results, however, it has not been studied for recovery of Si from secondary sources like EoL-Si. During the course of vacuum refining the volatile impurities (with vapor pressures higher than Si) will evaporate and leave the melt [27]. Recent industrial approaches in production of solar silicon by recovery of the Si kerf has shown minimum record of carbon footprint, 5 kg CO_2 equivalent emissions per kg of Si, while carbon footprint for standard Siemens method is higher than 100 kg CO_2. Recovery of Si from PV panels to a grade suitable for PV cells will save a lot of energy and reduce the carbon footprint of solar Si production [28]. Hence it is fair to expect a low carbon footprint and low power consumption process to produce solar cells via the recovery of Si from EoL-Si.

2. Experimental procedure

In this section, the details of the experimental work carried out on refining of Si are elaborated.

2.1. Starting material

The starting material used in this study was supplied by LOSER Chemie. Fig. 2(a) shows the isolated fragments of the Si solar cells. These shards carry the Ag front finger (the white lines on the blue facets), the diffused P layer, and the back layers. The Al back contact and silver fingers are removed by the LOSER chemistry process, which uses the treatment technique of aluminum chloride solution in the case of the aluminum [19] and for a second step the organosulfonic acids for the silver, providing a product shown in Fig. 2(b). As evident in Fig. 2(b), the treated Si pieces (known as demetallized Si in this study) still have the blue facet, indicating the remaining SiN_x layer.

2.2. Vacuum refining experiments

Vacuum refining experiments were carried out in a vacuum induction furnace. The details of the experimental setup is elaborated previously [29]. In order to evaluate the melting behavior of the input material, 30 g of the demetallized Si fragments was charged into a small graphite crucible (inner diameter 35 mm, IG-15, specifications can be found in Ref. [30]). The process was carried out in Ar atmosphere and before starting the process the chamber was vacuumed down to 7 Pa and flushed by Ar (6 N) for three times. The sample was heated up to 1500 °C and after holding for 10 min at that temperature the power was shut down and the crucible was let to cool down by itself. After the melting process, the crucible was cut in half and the solidified Si was studied by SEM-EDS technique. The refining process was also carried out in the same furnace, but in bigger crucibles (inner diameter 70 mm and height of 150 mm, grade IG-15, with the impurities Fe: 26, Ca: 6ppmw, V: 40, Al: 14, B: 3, and Ti: 33 ppmw). For the vacuum refining experiments 400 g of demetallized Si was charged in the crucible. A thermocouple Type C was applied for measuring the temperature during the experiment. Heating process was started by switching on the induction at a fixed frequency of 10.8 kHz. By reaching to around the melting point of silicon, the melting process started and after about 10–15 min all material was melted. All the heating and melting processes were carried out at 1050 mbar pressure of Ar atmosphere. At this point a sample was taken from the melt using quartz tube samplers (the details of the sample taking from melt are already elaborated in Refs. [31,32]) to measure the melt composition before the refining process. Then the chamber was vacuumed, and it was observed that when approaching the lower pressures much fume evaporated from the sample in crucible and by reaching pressure less than 100 mbar, lots of sparkles started erupting out of the crucible. The fume formation and sparkles eruption took place for almost 5 min and over the temperature range of 1500–1700 °C. Then the pressure in the chamber was reached to less than 100 Pa where the fume and sparkles were disappeared. The chamber was pressurized by Ar at this point and when reaching to the 1040 mbar Ar, another sample was taken from melt to check how this fume and sparkles formation affected on the melt composition and subsequently the experiment was stopped.

After cleaning the chamber from the fumes settled on the surfaces, the pre-refined material was then crushed and put in new crucible. The same procedure was carried out for setup preparation and the pre-refined material was melted in the crucible in Ar atmosphere, and then temperature was increased to 1800 °C, subsequently the chamber was vacuumed. This time no fume and sparkles were observed and once the pressure reached to 100 Pa, it was taken as the onset time of the vacuum refining process. during the vacuum refining process, the temperature was held consistent and after 30 min, the chamber was pressurized by Ar for taking sample from the melt. Having three steps of

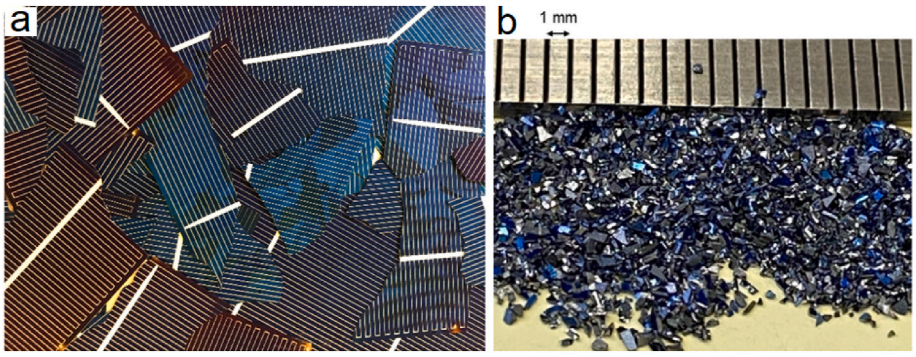

Fig. 2. (a): broken c-Si solar cell shards, with front side and back side. (b): the demetallized Si after being gone through the LOSER Chemie procedure for removal of Ag finger and Al back coating.

vacuum refining (and 90 min in total) we stopped the experiment and the rest of melt in the crucible was left to cool down, then the crucible was cut in half for further visual inspections.

2.3. Materials characterization

The silicon samples taken from the melt were digested in a mixture of HNO_3 and HF acids at room temperature, and then the obtained solution

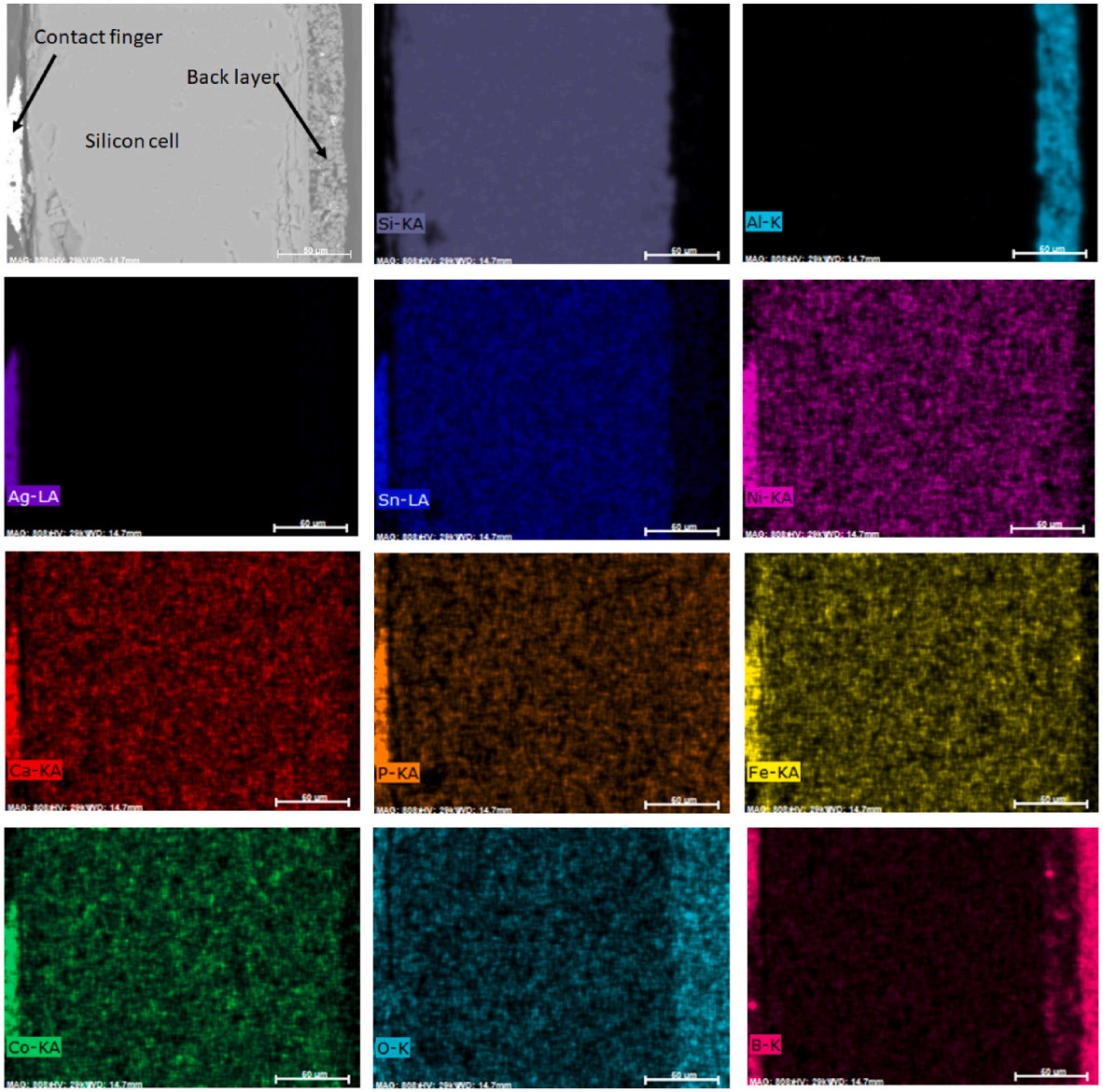

Fig. 3. The cross section of a c-Si cell under SEM and the corresponding EDS maps showing the distribution of various elements.

samples were analyzed by Agilent 8800 Triple Quadrupole ICP-MS (ICP-QQQ) with SPS 4 autosampler and quantified against standards from inorganic ventures and ^{115}In as internal standard. Three replicas were digested and measured by ICP-MS and the average numbers were considered for evaluating the refining process. The oxygen and nitrogen content of the samples, however, were measured by the inert gas fusion analysis method (IGFA, model ON836 made by LECO®, USA). The solidified refined silicon in the graphite crucible was cut in half and then

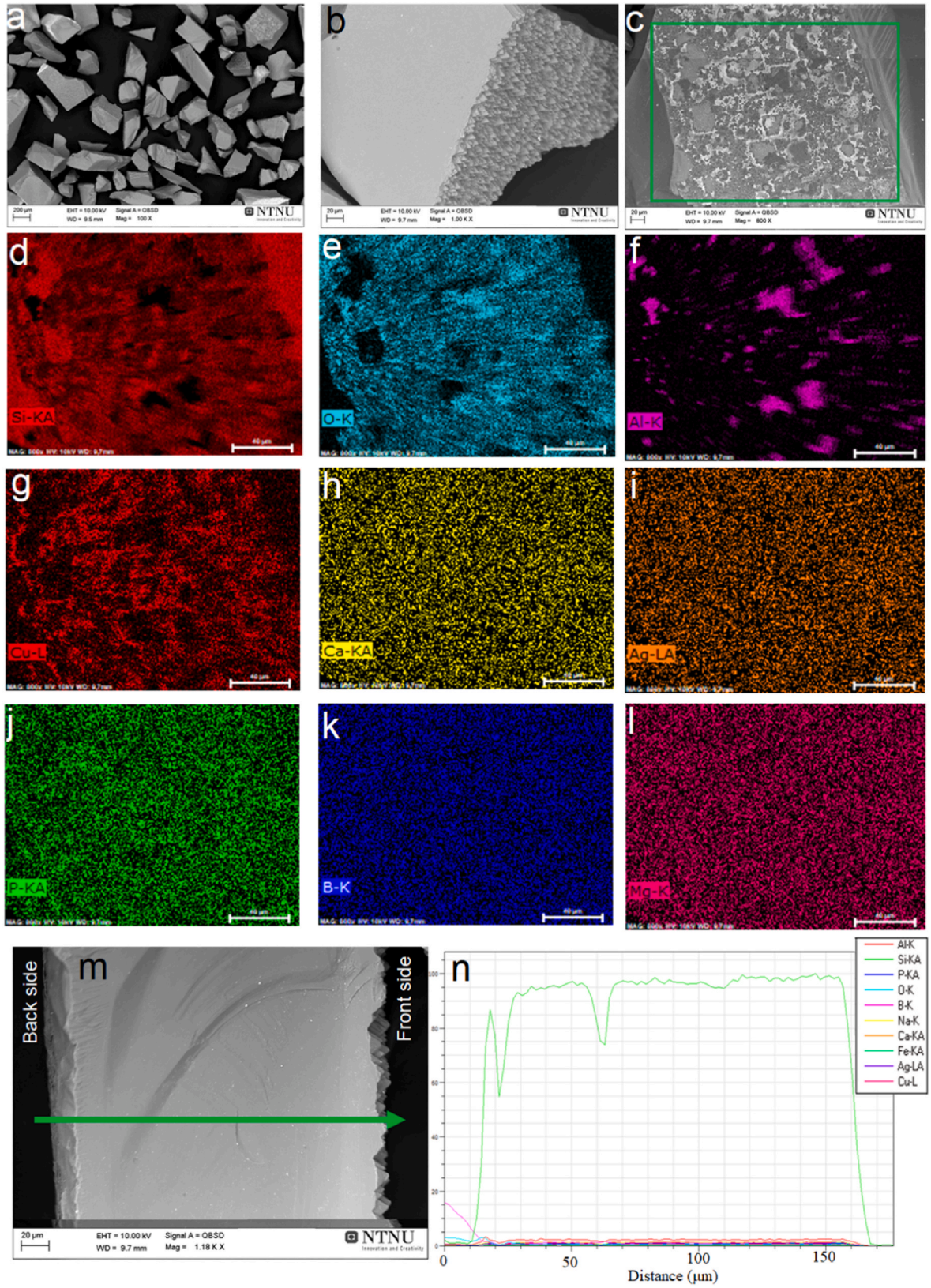

Fig. 4. SEM images of the demetallized Si fragments after acid etching by the LOSER Chemie process for removal of the silver contact finger and Al back layer.

sample were taken from the surface of the solidified ingot for Scanning Electron Microscopy (SEM, Zeiss Ultra 55, field emission).

3. Results and discussion

3.1. Characterization of the demetallized Si pieces

A photograph of the demetallized Si was already shown in Fig. 2(b), indicating that demetallized Si fragments have a blue facet, being the characteristic of the silicon nitride layer over the textured Si surface. This indicates the demetallized Si pieces have kept the silicon nitride layer even after the acid etching process. The SEM images of the shredded Si cells before the leaching process are presented in Fig. 3. The corresponding EDS maps showing the distribution of various elements are presented and they indicate that the back side layer is mainly Al, and the silver contact finger contains many impurities including Sn, Ni, P, Ca, Fe, and Co.

Fig. 4(a) shows the demetallized Si fragments after the leaching process. As obvious on the figure, these fragments have usually a length maximum 400–500 μm. A single Si fragment after the acid leaching is shown at higher magnifications in Fig. 4(b) where the front textured surface on this Si fragment is obvious. Fig. 4(c) also shows the back side of an acid treated Si fragment cell, which contains impurities. From Fig. 4(c) it seems that the Al layer is fully removed from the Si pieces, but it is the BSF layer that is still left on it. This image indicates the back oxide layer is not perfectly removed from all the Si pieces. The corresponding EDS maps of the same fragment is also presented in Fig. 4(d–l) indicating that the impurities on the back side of the Si piece contain Cu, Al, and O elements. The EDS maps show that aluminum oxides and copper oxides are still present on the backside and almost no other major impurities could be detected on the backside of the leached Si pieces. Many other impurities were included in the mapping (Ca, Ag, P, B, Mg, Ti), but they were not found as is obvious in Fig. 4(m, n). It can be concluded that the leaching process has been successful for the removal of the Al back layer and silver contact finger, but not completely successful for the removal of the BSF layer.

3.2. Melting of demetallized Si fragments

When melting the demetallized Si fragments, it was observed that the melt had a different specifications compared to the primary Si sources we already used for vacuum refining experiments, such as: Silgrain® [29], Ferrosilicon [33], FBR silicon alloyed with red phosphorus [34], a mixture of Silgrain® and Aluminum alloys [32]. When melting the demetallized Si fragments, we observed high amounts of fumes were formed in the crucible and out to the furnace chamber. Fig. 5(a) shows the solidified silicon has gotten a semispherical shape upon solidification, indicating that the graphite crucible was not wetted by the Si melt. According to literature [35,36] graphite is supposed to be wetted with Si and a contact angle about in between 15 and 25° is expected, depending to the graphite type. Therefore, the non-wetting observation may be due to a thin slag/oxide layer over the molten silicon, which is obvious in Fig. 5(b) on the solidified sample surface.

Fig. 6(a) represents the SEM image from the cross section of the solidified Si surface, where the surface oxide film is obvious. Fig. 6(b) depicts the surface of the Si at higher magnification and the corresponding EDS elemental mapping showing the distribution of the elements Ca, O, Al, Si, and P. Comparing the EDS elemental mapping in Fig. 6, it can be concluded that Ca–Si–O are staying together in the surface slag film. In addition, there is also an inclusion over the surface contain Ca–Al–O containing P. For the case of Al, this element is also dissolved in the Si, as it is expected from solutions thermodynamics point of view. The chemical composition of the as-received demetallized Si is presented in appendix (Table A-1 and Table A-2) showing high content of O and Ca. The oxygen content of the demetallized Si and the other impurities (specially Ca) reacted to form a thin slag layer over the Si melt. Although, Fig. 6 shows the thickness of this layer is micrometric, but it might have important effects on the physio-chemical properties of the system, as we observed, it prevents the wetting of graphite crucible by the liquid Si. Another important effect might be impurity absorption, P was dissolved in the Ca–Al–O inclusion shown in Fig. 6. The formation of slags from dissolved Ca and Al impurities in Si melt doing the oxidative ladle refining (OLR) process of metallurgical Si melt was discussed by Bjørnstad et al. [37,38]. Although, in the case of demetallized Si there is no oxygen blowing into the melt, the high content of the oxygen in the beginning material can associate with the metallic impurities and form the surface slag film. The slag formation will be discussed deeply in section 3.5.

3.3. Pre-refining and vacuum refining experiments

Having the experience from the melting experiment, the pre-refining experiment was done in a bigger graphite crucible filled by 400 g demetallized Si. The purpose of the pre-refining was to decompose the surface oxide layer and then provide a melt surface free of slag so the impurities could evaporate from the melt. Fig. 7(a–c) shows the crucible from above at elevated temperatures before, during, and almost at the end of the melting step, respectively. As shown in the figure, much fume formed during the melting process preventing good photography of the experiment, yet it could be recognized that the melt surface is not clean and a skim is observed on the melt, Fig. 7(a–c). Once the melting process was over, there was no solid Si pieces stuck over the graphite crucible wall, a sample was taken by plunging the sampler into the melt in 15 mm depth. Subsequently, the chamber was vacuumed, and the power was increased to start the pre refining process. It was observed that as the pressure reduced to lower than 100 mbar, the fume generation

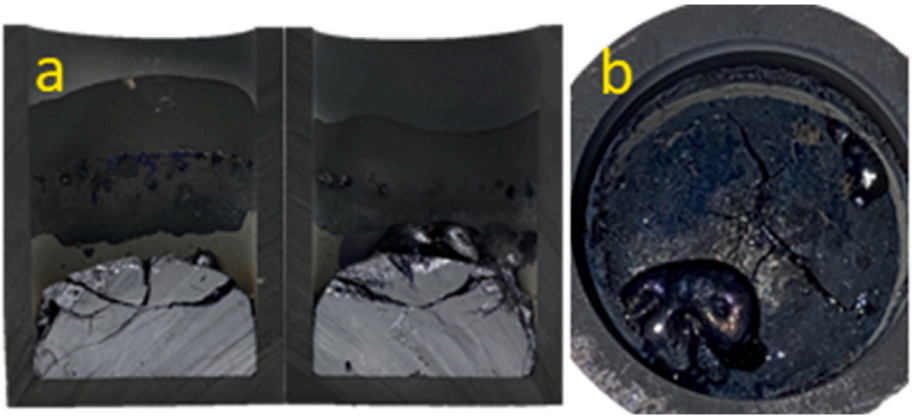

Fig. 5. The demetallized Si melted in Ar atmosphere and graphite crucible, (a: cross section, (b) surface of the solidified Si from above.

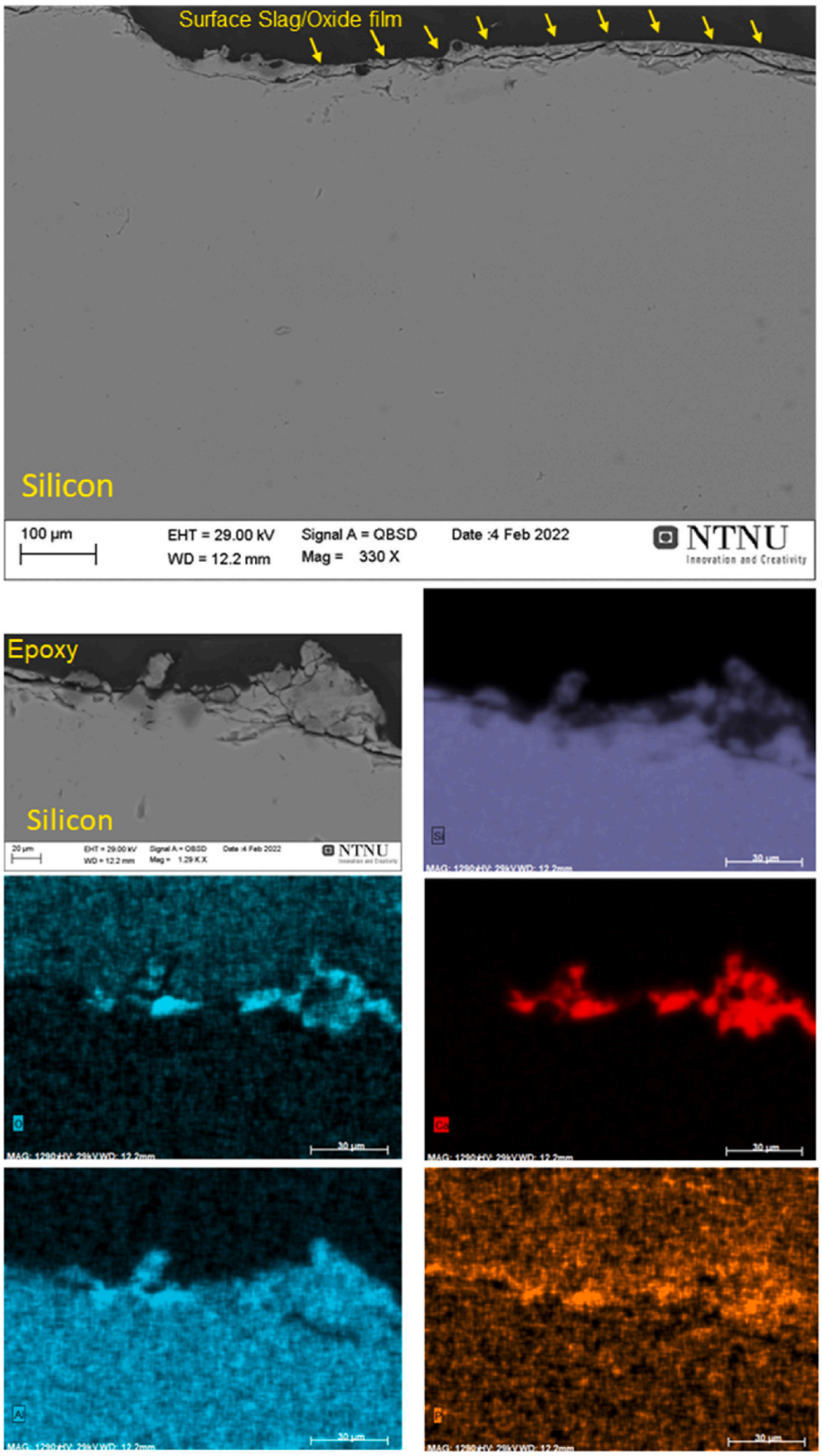

Fig. 6. SEM images from the cross section of the as melted demetallized Si and the EDS elemental mapping for Si, Al, O, Ca, and P.

intensified, Fig. 7(d–f), many sparks got thrown out of the crucible Fig. 7 (d). At this point the temperature was 1740 °C and then it was held consistent. By further reduction of the pressure in the chamber, the fuming became much faster and at lower pressures (20–25 mbar), the fume got an effusion shape. Fig. 7(f) shows the very last part of the fume effusion at a pressure about 1 mbar, some seconds after this step the fume generation and spark eruption were stopped. Top view of the melt indicated bubbling, with simultaneous sparks formation, see Fig. 7(g). When the pressure reached down to almost 1 mbar, sparking stopped and there was no fume anymore to effuse out of the crucible, the

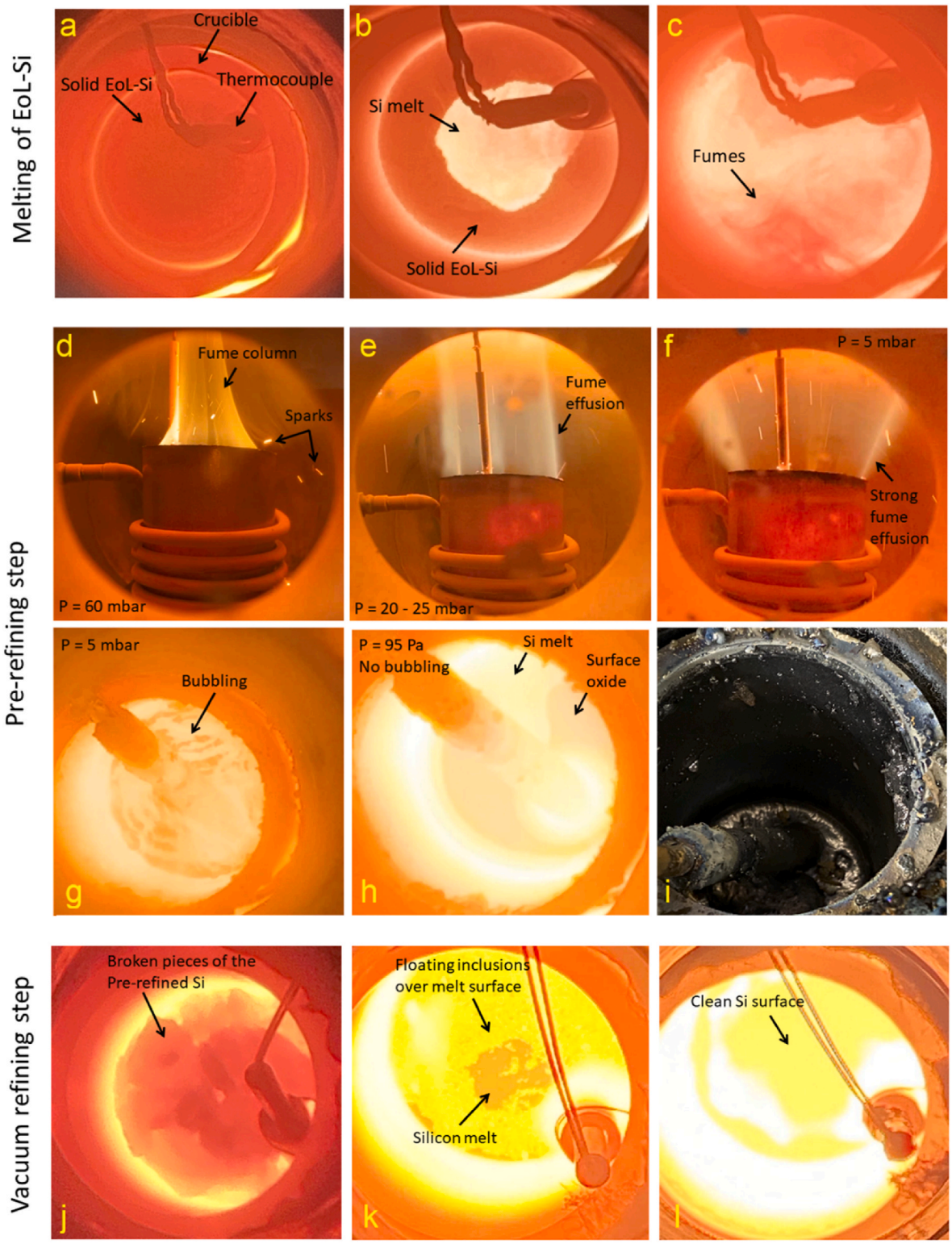

Fig. 7. Experimental observations of the melt and crucible at various status, (a): demetallized Si heated up to red hot temperature, (b): start of the melting process, (c): melting completed, (d–h): the pre-refining step at reduced pressures, (i): the solidified Si after pre-refining step, (j): the pre-refined Si re-melting, (k): the melted pre-refined Si, (l): melt surface of the silicon after the vacuum refining.

bubbling over the melt surface stopped as well and a stagnant melt surface was recorded, as shown in Fig. 7(h). The figure indicates that the melt surface has two different parts, the darker side indicates there are still some oxide/impurities over the melt surface. Up to this stage lots of condensate was formed and sampling was not possible. Therefore, the experiment was stopped, and the melt was cooled down and solidified in the crucible. The melt that has gone through this pretreatment will be known as the pre-refined melt. Fig. 7(i) shows the crucible after the solidification and the pre-refining process and as can be seen there are many Si droplets splashed over the upper parts of the crucible wall. The crucible was crushed, and the solidified Si was separated, re-charged into a new graphite crucible, and was heated up in the furnace. Fig. 7

(j) shows the pre-refined Si lumps right before the melting starts. Once the sample was melted, some solid particles were observed floating over the melt surface, Fig. 7(k), at this point a sample was taken from the melt to measure a representative composition of the pre-refined silicon. Subsequently the vacuum refining process was started by vacuuming the chamber and increasing the temperature up to 1800 °C. The vacuum refining process was carried out for 90 min, while samples were taken from the melt every 30 min. Fig. 7(l) shows the final state of the melt indicating the melt surface is clean.

3.4. Impurities removal

The average values of the impurities are plotted in Fig. 8 during both pre-refining and vacuum refining steps. Considering the concentration and the nature of the impurities presented in Table A-1 and Table A-2, we can sort the impurities of the demetallized Si into three sub-categories, as follows.

- Metallic impurities: major impurities (>100 ppmw, Ca, Ag, Sn) and minor impurities (<100 ppmw Ti, Cu, Ni, Al, Fe, Cr, V, Mg).
- Dopant impurities: P and B.
- Dissolved gasses: O and N.

The most abundant impurities in the demetallized Si are oxygen (0.37 wt%), Calcium (0.28 wt%), and then Nitrogen (0.11 wt%). The considerable amount of oxygen could be due to the surface oxidation of the silicon shards during the leaching and acid treatment processes carried out to remove the Ag and Al from the Si surfaces. We already showed in Fig. 3 that the printed silver finger contains many impurities and hence it can be the source of all these impurities in the melted Si. Although the main part of the silver contact layer is removed by acid leaching [10], it is expected that some Ag and other impurities from the silver paste are diffused to the Si bulk during the firing step being done over 600–700 °C for providing the contact of screen-printed silver with the Si substrate. Hence the high content of the Ca could originate from the silver paste. Another possible source for Ca might be small pieces of glass, and also $CaMgSiO_4$ impurities from the back side Al layer [9], left in the material. The Al and Cu, however, were detected on back side of the demetallized Si, Fig. 4, and hence with having 100 ppmw, could be originated from the back layer of the silicon solar cells. Nitrogen, however, is expected from the SiN_x anti-reflection layer that is over the front surface of the Si solar cells. Phosphorus comes from the n^+ emitter layer (P diffused layer) for making the p-n junction and B is the doping element in the P type solar cells.

Fig. 8(a) depicts the changes in the concertation of most abundant impurities, Ca, O, and N elements over the pre-refining and vacuum refining processes. This figure indicates that the concentration changes for the Ca, O, and N elements in the melt have correlation. Once the Si is melted in the crucible, the concentration of the Ca, O, and N in the melt reduces considerably while after the pre-refining step increases. The concentration of N also reaches zero in the melted Si and after the pre-refining process increases again. As we mentioned in the experimental section, the chamber is fully vacuumed and flushed by Ar before experiment, therefore the increase in the O and N content in the melt is a characteristic of the melt and cannot be due to any extrinsic issue. Considering the slag/oxide film that forms over the melted Si, Fig. 5(a and b) and the SEM images shown in Fig. 6, a good correlation can be seen between the formation of the slag layer over Si and the decrease in concentration of Ca, O, and N elements in the melt, and its disappearance from the surface and the increase of the O and N concentration in the melt. This is valid for the rest of metallic impurities in the melt, with the exception for P and Mg. In section 3.5 we interpret the results.

It is worth to mention that when taking the last sample from the melt, a shorter sample taker was used and during the sample taking process, the quartz tube barely reached to the surface of the melt. Therefore, the last sample was taken from surface of the melt and hence it can be seen that some of the impurities (Ti, Ni) have higher concentrations, but O is considerably higher.

The concentration changes of the major metallic impurities (Ag and Sn) in Fig. 8(b) shows their concentrations are almost the same in the as-received Si and the melted material. As it is obvious in Fig. 2, the silver screen is printed over the PV cell and the contact finger is printed in form of parallel lines on the Si solar cells, therefore only few of the crushed pieces contain the silver contact finger. Therefore, when taking sample

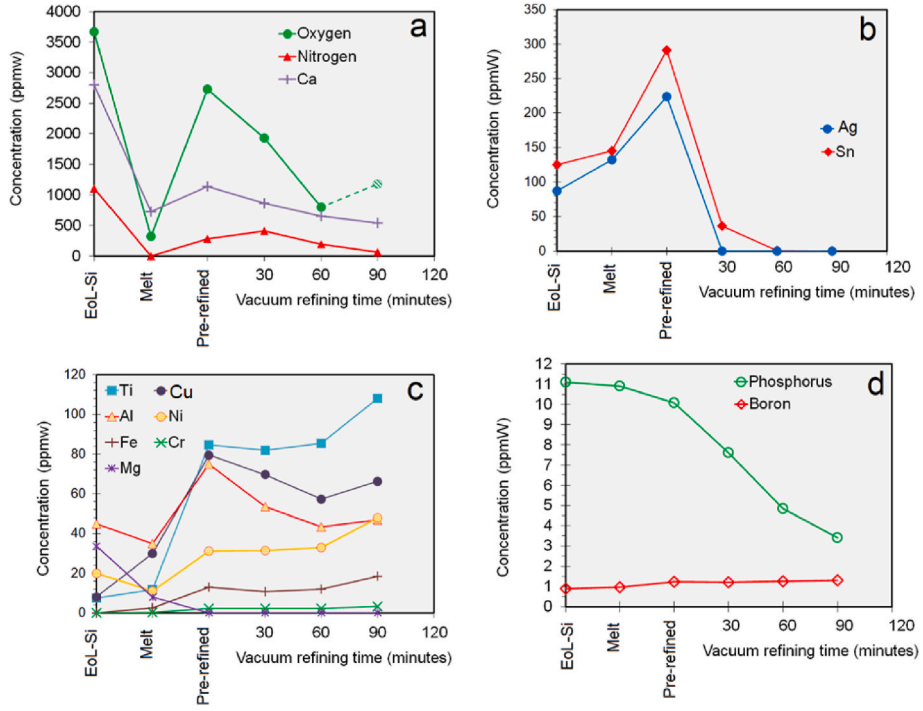

Fig. 8. Change of Impurities' concentration in Si melt in various steps of refining process.

from the as received demetallized Si pieces, a homogenous sample from the material is not guaranteed, and there is a high chance to have more of the pieces without the Ag contact finger on. This might explain the reason that the Ag and Sn concentrations is slightly higher in the melted Si compared to as-received Si. The same the other impurities, after the pre-refining process the Ag and Sn concentrations have increased in the melt. Subsequently, during vacuum refining the concentrations of both Ag and Sn reduces dramatically and as it is obvious in Fig. 8(b), after only 30 min, Ag is fully removed from the melt, while Sn requires 60 min to evaporate completely. The dopant impurities (P and B), however, behave differently than the metallic impurities, Fig. 8(c). Phosphorous concentration reduces continuously during both pre-refining and vacuum refining processes. In addition, the B content is steady all over the refining process, which was expected since it is not supposed to evaporate during vacuum refining neither can be absorbed efficiently by the Si–Ca–O slags. From Fig. 8(d), it is obvious that the same as the major impurities, the concentration of the minor metallic impurities first reduces by melting the Si, and subsequently increases after the pre-refining process, but their concentrations are not significantly changed over the course of vacuum refining. The only two minor impurities that can be removed from the melt are Al (partially removed) and Mg (fully removed in the pre-refining process). The rest of the minor metallic impurities, however, does not evaporate from the melt and their concentration is almost steady over the vacuum refining time.

The presented results in this section showed that vacuum refining led to the removal of considerable amounts of Ca and its concentration reduced from 2803 ppmw to 539 ppmw, and a full removal of Ag, Sn, and Mg was observed under applied conditions. Evaporation of various elements from the Si melt can be studied theoretically by calculating the volatility coefficient (α_i) for each element, as done previously [27]. The higher the value for volatility coefficient, the better the removal of the element from Si melt in vacuum refining process [32]. The α_i over temperature range of 1414–2000 °C as follows: $\alpha_P > \alpha_{Pb} > \alpha_{Mg} > \alpha_{Ca} > \alpha_{Ag} > \alpha_{Sn} > \alpha_{Al} > \alpha_{Cu}$. The experimental results are in good agreement with these theoretical calculations, as for the case of Ag and Sn with almost the same concentrations in the melt, Ag was fully evaporated in 30 min and then Sn was gone in 60 min of vacuum evaporation. Although Ca has a higher α_{Ca} value, but due to its high concentration in the melt longer times of refining is required. However, the sudden increase in the concentration of the elements after the pre-refining process requires further interpretation and it will be discussed in section 3.5.

3.5. Interpretation of the vacuum refining results

The obtained results from the vacuum refining process can be interpreted using the required thermodynamic calculations with FactSage [39] software. The first thing that needs to be explained is the sudden increase of the impurity concentrations after the pre-refining step. Especially for the case of the O and N we showed once the material is melted their concentration reduces dramatically in the melt and then again increases after the pre-refining step. The in-situ photography of the pre-refining experiment and the images of the melted Si (Fig. 5) indicated a thin slag/oxide layer formed over the Si, which gets decomposed and evaporates during the pre-refining step. Considering the high content of the Ca and O in the material, one can assume the formation of a slag layer in the CaO–SiO_2 system floating over the Si melt.

Using FactSage software and inputting the measured amounts of Si, Ca, and O, an equilibrium assessment has been done. The rest of the impurities were not considered in the calculations since they will be solute elements in the slag and Si system and considering their low concentration an exact calculation requires the right thermodynamic database. The stable phases under the experimental conditions (1 bar) are liquid Si, liquid slag (slag A#1), and solid SiO_2 and $CaSiO_3$ phases, depending on the Ca and O contents in the Si raw materials, as shown in Fig. 9. For obtaining Fig. 9(a and b), the chemical composition of the as-received Si (with 0.28 wt% Ca) was used for the thermodynamics calculations, and therefore these figures represent the calculated melt/slag compositions in the melted Si, and at various temperatures. However, for the calculations of Fig. 9 (c and d), we used the chemical composition of the melt after the pre-refining process (0.11 wt% Ca). Fig. 9(a) shows the existence of solid $CaSiO_3$ and SiO_2 particles over the melt once the Si is melted and then by the increase of the temperature, a slag (slagA#1, 2.3 g) will form in the system. According to Fig. 9(b) the CaO content of the slag A#1 reduces with increasing temperature, while the Ca content increases in the melt, which means Ca mass transport to Si melt via CaO dissociation/reduction with increasing temperature. To evaluate the melt compositions of the pre-refined Si, the melting of 300 g of demetallized Si was simulated, and it yields 1.4 g of solid SiO_2 and approximately 0.5 g of liquid slag A#1 (Fig. 9(c)). However, at temperatures higher than 1650 °C the solid SiO_2 becomes unstable and liquid slag A#2 appears in the system. However, at elevated temperatures and beyond 1800 °C the content of both liquid slags in the system start to decline and

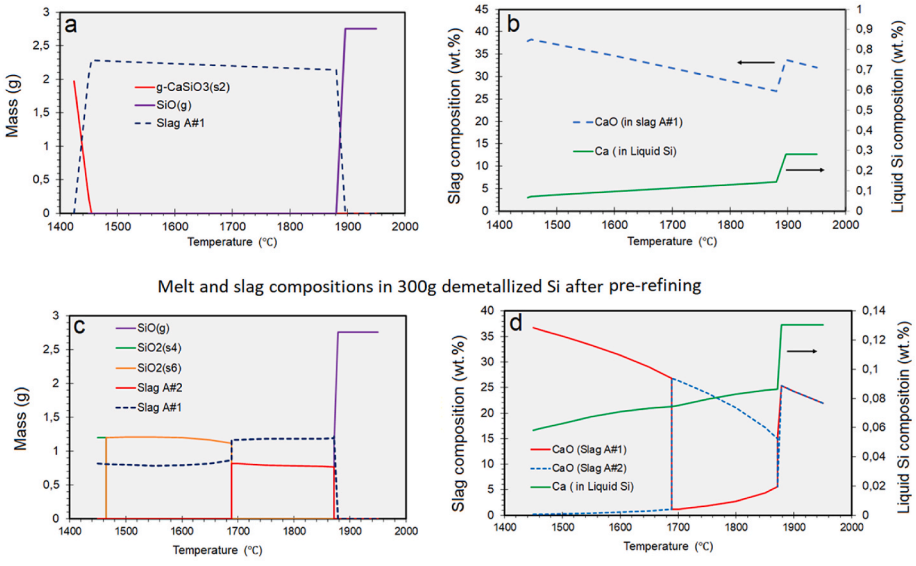

Fig. 9. The stable phases in equilibrium with liquid Si when melting 300 g demetallized Si (a and b), and the stable phases in equilibrium with the Si melt after the pre-refining process.

$SiO_{(g)}$ forms in the system. In another word, by increasing the temperature, SiO_2 in slag react with liquid silicon and form $SiO_{(g)}$. Fig. 9(d) represents the slag/melt composition for the pre-refined Si and indicates the CaO content of the slag reduces by elevating temperature which accompanies by the increase of Ca in the melt. Up to here, we can see that the Ca concertation in the melt has a correlation with the CaO content of the slags.

The same equilibrium calculations were carried out considering the Ca and O content of the demetallized Si at the reduced pressure of 1 mbar, to calculate the stable phases in equilibrium with liquid Si in vacuum conditions. The results in Fig. 10(a) indicate no slag or solid silicon oxide phases stable at this pressure. All the O content of the material is transferred to the gas phase in form of SiO gas. The gas phase in addition to SiO contains lower levels of Ca vapors at elevated temperatures ($T > 1900$ °C).

The thermodynamic calculations presented here, can explain all the phenomena observed in the melting process of the demetallized Si including the slag/oxide layer formation over the melt and the fume and sparking phenomena observed during the pre-refining process. The thermodynamic evaluations are in good agreement with the in-situ observations shown in Fig. 5(a and b), where a thin slag layer over the melted Si was obvious. Both the slags and the solid SiO_2 will float over the surface of Si melt which prevents the crucible to be wetted by Si melt, and hence provides a hemisphere shape for the unrefined melted Si in the crucible.

Based on the thermodynamic assessment of the system, approximately 0.67 wt% of the melted Si will convert to the slag and solid SiO_2 (almost 2g from 300g) which floats over the Si surface. This slag film can absorb some impurities, as shown schematically in Fig. 11(a). This figure also indicates when the slag/oxide layer exist on the Si melt, there is no wetting between the graphite crucible and the melt, leading to the convex shape of the melt in crucible. However, during the pre-refining step, this slag layer will get decomposed at lower pressures to form $SiO_{(g)}$. Fig. 11(a) also shows the $SiO_{(g)}$ formation is accompanied by bubbling in the melt and once the bubbles burst over the surface, small droplets of melt/slag will be thrown away of the crucible. By the decomposition of the slag layer, those impurities that are collected in the slag/oxide layer will return to the melt, as shown in Fig. 11(b). We indicate here that after the pre-refining process the slag layer is mainly gone and one cannot assume the solid SiO_2 to be present in the system, but this figure indicates that there is still high content of the O left over the melt surface. When doing the vacuum refining for P removal, we already have shown that the rate of the process will be controlled mainly by the evaporation at the melt surface and diffusion in the gas phase. When comparing the rate of phosphorus removal from the demetallized

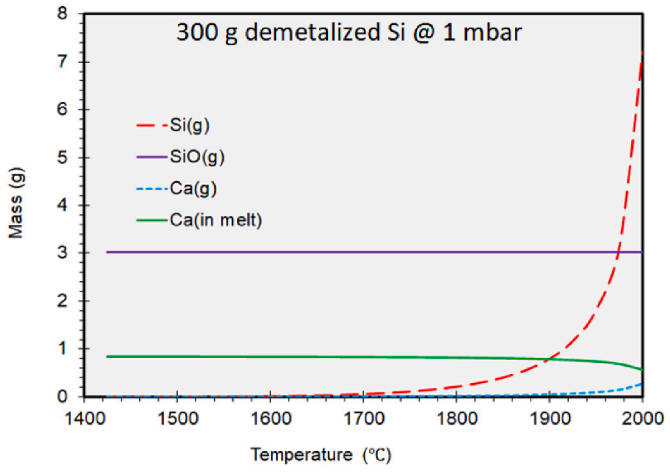

Fig. 10. Thermodynamics calculations showing the stable phases in equilibrium with liquid Si (no slag is stable at this pressure).

Si melt with other clean melts like Silgrain® [29] and FBR® silicon alloyed with P [34], Si–P alloy with 92.7 ppmw phosphorus at 1800 °C, only 80 min was required to remove phosphorus to below 0.2 ppmw. However, according to Fig. 8(c), over the course of the vacuum refining process, P content of the Si melt reduced from 10.1 ppmw to 3.4 ppmw, standing for 66.3 wt% P removal after 90 min of refining at the same temperature. For the case of B, the concentration slightly increases in the pre-refining step (from 1 to 1.25 ppmw) and then is almost steady over the course of the vacuum refining. Having the surface oxide film over the melt, and the inclusion that we already showed in Fig. 8(a), the evaporation of elements will have a lower rate compared to the melts with a perfectly clean surface. We already mentioned the last sample was taken from the melt surface and it was shown in Fig. 8(a) that this sample consists of considerable amount of oxygen. This might explain why the rate of P removal from Si was considerably slower than the clean melts [27,29,31–34,40].

Based on the thermodynamic calculations presented here, the following reactions can be suggested for the formation of the slag layer over the melt:

$$x\mathrm{CaO} + y\mathrm{SiO_2} = (xCaO.y\mathrm{SiO_2})_{\mathrm{Slag}} \quad (1)$$

where x and y are stoichiometric coefficients for CaO and SiO_2 in the slag. then during the pre-refining step when the pressure of the chamber is decreased, the SiO_2 will decompose thorough these steps:

$$(\mathrm{SiO_2})_{\mathrm{slag}} = \mathrm{Si_{(l)}} + 2\mathrm{O} \quad (2)$$

$$\mathrm{Si} + \mathrm{O} = \mathrm{SiO_{(g)}} \quad (3)$$

Where the reaction (3) explains that each SiO_2 introduces one Si and two dissolved oxygen (O) into melt, and then one Si and O are required to associate to form SiO gas. Therefore, the overall reaction for the decomposition is:

$$\mathrm{SiO_2} = \mathrm{SiO_{(g)}} + \mathrm{O} \quad (4)$$

Which explains the decomposition of 1 mol SiO_2 (present in slag layer or in form of S4 or S6 solids), introduces 1 mol O to the melt and this can explain the increase in the oxygen content of the melt after the pre-refining step. Additionally, the CaO content of the slag also can decompose with the same mechanism to form $Ca_{(g)}$ as follows:

$$\mathrm{CaO} = \mathrm{Ca_{(g)}} + \mathrm{O} \quad (5)$$

$$\mathrm{Ca} = \mathrm{Ca_{(g)}} \quad (6)$$

Where Ca is the dissolved Ca in liquid Si. The reactions (4) and (5) indicate that by decomposition of the SiO_2–CaO slag system, the concentration of dissolved oxygen in melt increases, and this can explain the oxygen increase in the melt after the slag decomposition in the pre-refining step. This oxygen will then be removed by the end of vacuum refining experiment though the formation of $SiO_{(g)}$ and by carbon monoxide formation:

$$\mathrm{C} + \mathrm{O} = \mathrm{CO_{(g)}} \quad (7)$$

Where C is the carbon dissolved in Si melt from graphite crucible, associating with the dissolved oxygen to form CO. As long as there is oxygen in the Si melt, one can assume a think surface oxide film over the melt, slowing down the evaporation kinetics of the impurities from Si.

4. Vacuum refining for recycling of EoL-Si

This research showed vacuum refining is a proper process for the recovery of Si from EoL-Si. Results showed N, Ag, Sn were completely removed, while more than 68.4% P, 52.5% Ca, and 37.5% Al were removed (as shown in Fig. 8). Phosphorus removal to acceptable levels is

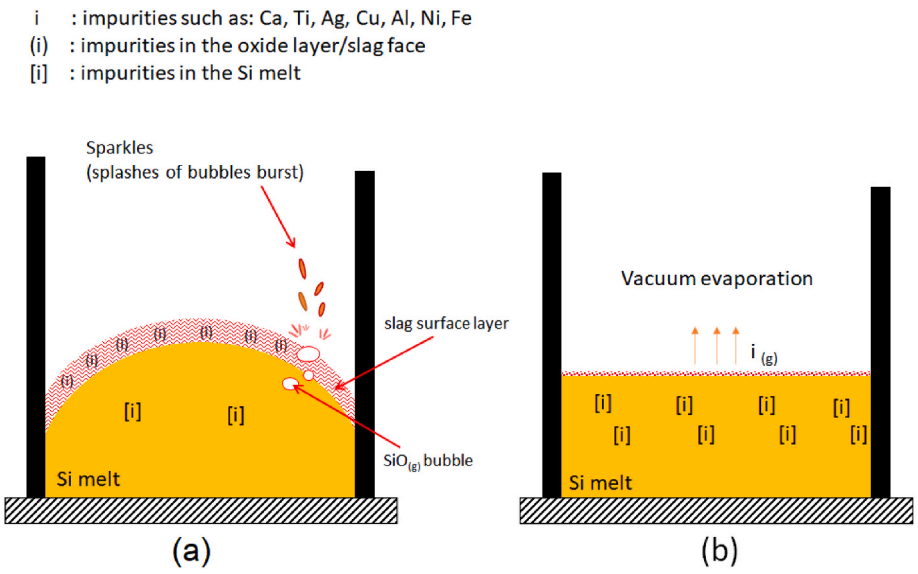

Fig. 11. The schematic figures representing the surface oxide/slag layer over the molten silicon. (a): the surface oxide film in atmospheric pressures containing impurities, (b): the decomposition of the oxide film at lower pressure by formation of $SiO_{(g)}$ bubbles.

necessary since it is the doping element and if remained in the Si, will lower the solar cell efficiency, and more removal is possible as has been experienced [29]. Vacuum refining did not work for the removal of B, Fe, Ti, Ni, Cr, but these elements (except B) will be effectively removed in the subsequent directional solidification step in the keychain of the Si solar cell production as their concentrations is low. Table 1 shows the segregation coefficient (K) value for the remined metallic impurities, collected from Ref. [41]. The obtained impurity concentrations of Si after vacuum refining, and the expected impurity level in Si to be achieved after directional solidification are shown in the table. The initial concentrations of the impurities in the demetallized Si and after the vacuum refining is presented in Table 1. By considering the equilibrium segregation coefficient for each element and Scheil equation [41] (the details of calculations can be found in the supplementary file), the remained amount of each element after a single directional solidification is calculated for two scenarios.

(a) Starting directly from demetallized Si without vacuum refining
(b) After vacuum refining of the demetallized Si

Table 1 shows without vacuum refining of demetallized Si, it is not possible to reach the SoG-Si, specially due to having high contents of elements P, N, Ca, and B, however after applying the vacuum refining process, all the elements are in the acceptable range of impurities mentioned in Ref. [42]. It is worth to mention here that any remained amount of P, Ca, and N, can be removed fully from the melt at longer times of vacuum refining. However, for the case of B, if removal of B from 1.3 ppmw to less than 0.1 ppmw is required, the gas refining process will be best candidate [43,44]. Gas refining is also able to remove B thoroughly. The other solutions for B, could be mixing of the recovered Si with new SoG-Si to dilute the B content or make PV cells by

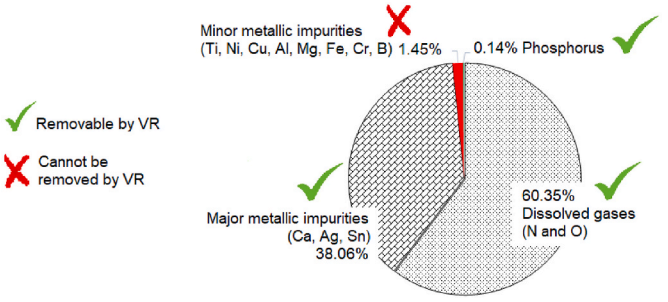

Fig. 12. The pie chart showing the extent of various impurities type in the demetallized Si and the required treatments (VR: vacuum refining).

Table 1
An estimation of remained impurities in Si ingot after the refining and directional solidifications process (VR: Vacuum refining, DS: directional solidification).

Impurity element	As-received material	After Vacuum refining	Equilibrium segregation coefficient [41]	Without VR and after DS (10% top cut)	Meeting SoG-Si feedstock limits [42]	With VR and DS (10% top cut)	Meeting SoG-Si feedstock limits [42]
	ppmw	ppmw	K	ppmw		ppmw	
Fe[a]	<E−02	18.52	8.00E-06	<E−02	Yes	<E−02	Yes
Cu[a]	8.16	66.40	8.10E-04	<E−02	Yes	<E−02	Yes
Ti[a]	7.63	108.20	2.00E-06	<E−02	Yes	<E−02	Yes
V[a]	0.09	2.80	4.00E-06	<E−02	Yes	<E−02	Yes
Cr[a]	0.09	3.30	1.10E-05	<E−02	Yes	<E−02	Yes
Ni[a]	20.00	47.90	1.30E-04	<E−02	Yes	<E−02	Yes
B[a]	0.90	1.30	0.80	0.85	Yes	1.23	Yes
Al[a]	45.33	46.6	3.10E-02	3.58	Yes	3.68	Yes
Ag	87.50	<E−02	1.7E-05	<E−02	Yes	<E−02	Yes
P	11.33	5.60	0.35	7.19	No	2.16	Yes
N	1110.00	64.00	7.00E-03	2.10	No	0.12	Yes
Ca	2803	373.00	1.60E-03	12.24	No	2.33	Yes

[a] The concentration of these elements increased by contamination from crucible (see graphite crucible specification used in this research).

the compensation technique, or keeping required amount of P in Si so these two elements can compensate each other's effects [14,15,45]. Fig. 12 shows a pie chart categorizing the impurities and showing which one can be removed by which process. The figure indicates all the impurities in the demetallized Si is 0.7920 wt%, from which 0.7794 wt% (standing for 98.55% of all impurities) are the volatile impurities that can be removed by vacuum refining, indicating on the importance and efficiency of this process for the recovery of SoG-Si from EoL-Si.

Fig. 13 represents a process for the valorization of the EoL-Si to produce PV-Si (a Si product appropriate to be used in photovoltaic), including the vacuum refining and directional solidification. As shown on the figure, the evaporated Ag and Sn can be later recovered from the fumes of the process through various approaches. Assuming the oxygen removal by means of $SiO_{(g)}$ formation, then it can be calculated that for the removal of 0.367 wt% oxygen from the melt, 0.64 wt% Si of the silicon will be converted to $SiO_{(g)}$, making a silica equivalent to the 1.01 wt% of the melt. By considering a full evaporation of Ca, Ag, and Sn (equivalent to 0.301 wt% of the melt), about 9 kg fumes will be generated per metric ton of EoL-Si which will be rich in Ag and Sn, with the concentrations of 2.48 wt% and 3.2 wt%, respectively, and can be used for recovery of these elements. The theoretical power consumption for vacuum refining of Si is already presented in Ref. [29], and it is shown for refining of a Si containing 10 ppmw P, 2.5 kWh per kg of Si is required.

5. Conclusions

In this paper vacuum refining process was tried to recover solar Si from the demetallized Si cell. Promising results are achieved, and the following remarks can be summarized from the research.

- The demetallized EoL-Si contains high content of N, O, and Ca impurities in 1000–3500 ppmw level.
- Source of impurities are accused to be the remained BSF oxide layer and the impurities from the silver contact finger, being diffused to the Si surface in the firing step.
- Once the demetallized EoL-Si was melted, a slag/oxide layer was formed over the Si melt and this layer was successfully decomposed in the pre-refining step at reduced Ar pressures.
- Vacuum refining of the input Si at 1800 °C led to the complete removal of N, Ag, Sn, and more than 68.4% P, 52.5% Ca, and 37.5% Al over the applied time, which later can be removed at longer times.
- A process candidate for the recovery of EoL-Si using vacuum refining and directional solidification was proposed.
- A flue gas and then a condensate is generated through the initial stages of vacuum refining, and it may be a secondary source of Ag and Sn.

CRediT authorship contribution statement

Arman Hoseinpur: Visualization, Methodology, Investigation, Formal analysis, Data curation, Conceptualization, Validation, Writing – original draft. **Kai Tang:** Writing – review & editing, Software. **Alexander Ulyashin:** Funding acquisition, Conceptualization, Project administration, Writing – review & editing. **Wolfram Palitzsch:** Resources. **Jafar Safarian:** Writing – review & editing, Resources.

Declaration of competing interest

The authors declare that they have no known competing financial interests or personal relationships that could have appeared to influence

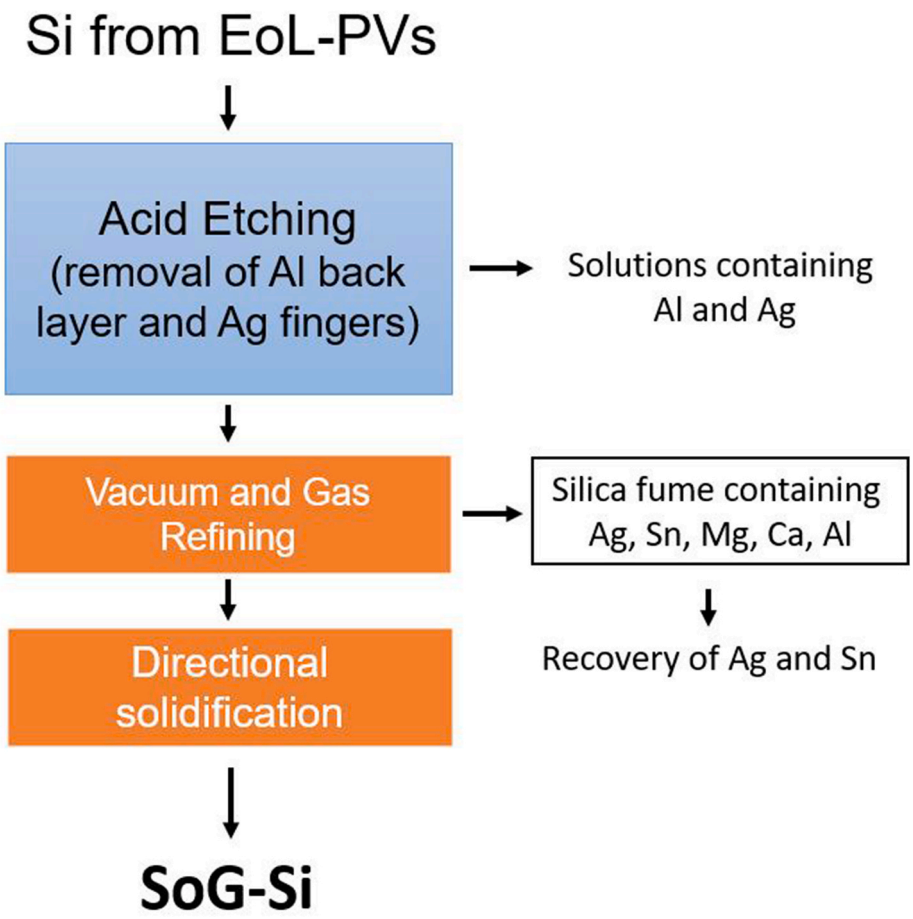

Fig. 13. The proposed process for valorization of EoL-Si up to SoG-Si.

the work reported in this paper.

Data availability

all the data are presented in the text

Acknowledgments

The work has been carried out in the Research Centre for Sustainable Solar Cell Technology (FME SuSolTech, project number 257639) in Norway. The European project SuperPV-WP3 (102018516—3) is appreciated for covering the experimental costs. LOSER Chemie is appreciated for supply of the demetallized Si.

Appendix A. Supplementary data

Supplementary data to this article can be found online at https://doi.org/10.1016/j.solmat.2023.112181.

Appendix

Table A-1
The impurities concentration in the as-received EoL-Si and in the samples taken from melt, using ICP-MS technique.

Sample	B	Mg	Al	P	Ca	Ti	V	Cr	Fe	Ni	Cu	Ag	Sn
As-received demetallized EoL-Si	1.0	28	30	12	2804	5.7	<0.096	<0.096	<0.02	12	5.3	84	121
	0.9	24	63	10	2998	12	<0.091	<0.091	<0.02	24	10	90	129
	0.8	49	43	12	2607	5.2	<0.082	<0.082	<0.02	24	9.2	87	123
As melted EoL-Si	1.0	11	21	10.5	829	14	<0.04	0.34	1.0	13	38	164	172
	1.1	6.3	29	11.1	739	14	<0.06	0.39	1.2	13	35	161	168
		<6.8	34		624	7.5	<0.07	0.32	5.3	6.8	17	71	96
Pre-refined	1.3	<5.9	37	10.4	964	59	0.86	1.6	14	20	48	144	195
	1.2	<52	77	9.8	1150	85	1.3	2.3	11	33	80	230	294
		<5.3	111		1294	110	1.6	3.0	14	40	110	298	385
Vacuum refined	1.3	<5.9	37	7.7	818	71	1.3	1.8	8.7	26	55	1.0	31
30 min	1.2	<5.2	48	7.5	825	79	1.4	2.3	11	31	63	1.1	35
		<5.3	76		952	96	1.7	2.6	12	38	91	1.5	44
Vacuum refined	1.3	<6.1	39	4.3	633	80	1.8	2.2	12	32	56	<0.06	0.66
60 min	1.2	<5.2	41	5.4	641	84	1.9	2.3	11	32	55	<0.05	0.67
		<5.0	50		678	92	2.1	2.5	13	36	62	<0.05	0.73
Vacuum refined	1.3	<5.3	45	4.0	535	106	2.7	3.2	17	45	63	<0.05	<0.03
90 min	1.3	<5.7	47	2.8	555	107	2.8	3.0	15	50	67	<0.06	<0.03
		<5.9	48		529	112	2.9	3.7	24	49	69	<0.06	<0.03

Table A- 2
Oxygen and nitrogen content of the samples measured by IGA method (* this sample is biased and the reason is elaborated in the text).

Sample name	Oxygen (wt.%)	Nitrogen (wt.%)
As-received EoL-Si (demetallized)	0.367	0.111
Melted EoL-Si	0.0325	0.000
Pre-refined	0.273	0.0289
Vacuum refined 30 min	0.193	0.0415
Vacuum refined 60min	0.079	0.0196
Vacuum refined 90 min*	0.118*	0.0064*

References

[1] A. Cuthbertsen, World passes 1TW of solar installations - enough to power the whole of Europe, Independent (2022). https://www.independent.co.uk/tech/solar-power-renewable-energy-europe-b2036988.html. (Accessed 25 May 2022). accessed.
[2] J.F. Weaver, World Has Installed 1TW of Solar Capacity, PV-Magazine, 2022. https://www.pv-magazine.com/2022/03/15/humans-have-installed-1-terawatt-of-solar-capacity/. (Accessed 25 May 2022). accessed.
[3] K. Komoto, J.S. Lee, End-of-Life Management of Photovoltaic Panels: Trends in PV Module Recycling Technologies, 2018. Report IEA-PVPS T12-10: 2018, ISBN 978-3-906042-61-9.
[4] M. Peplow, Solar panels face recycling challenge, ACS Cent. Sci. 8 (2022) 299–302, https://doi.org/10.1021/acscentsci.2c00214.
[5] T. Maani, I. Celik, M.J. Heben, R.J. Ellingson, D. Apul, Environmental impacts of recycling crystalline silicon (c-SI) and cadmium telluride (CDTE) solar panels, Sci. Total Environ. 735 (2020), 138827, https://doi.org/10.1016/j.scitotenv.2020.138827.
[6] M.M. Lunardi, J.P. Alvarez-Gaitan, J.I. Bilbao, R. Corkish, A review of recycling processes for photovoltaic modules, in: Sol. Panels Photovolt. Mater., InTech, 2018, pp. 137–144, https://doi.org/10.5772/intechopen.74390.
[7] G. Ansanelli, G. Fiorentino, M. Tammaro, A. Zucaro, A life cycle assessment of a recovery process from end-of-life photovoltaic panels, Appl. Energy 290 (2021), 116727, https://doi.org/10.1016/j.apenergy.2021.116727.
[8] V.A. Popovich, M. Janssen, I.M. Richardson, T. van Amstel, I.J. Bennett, Microstructure and mechanical properties of aluminum back contact layers, Sol. Energy Mater. Sol. Cells 95 (2011) 93–96, https://doi.org/10.1016/j.solmat.2010.04.037.
[9] V.A. Popovich, M.P.F.H.L. van Maris, M. Janssen, I.J. Bennett, I.M. Richardson, Understanding the properties of silicon solar cells aluminium contact layers and its effect on mechanical stability, Mater. Sci. Appl. 4 (2013) 118–127, https://doi.org/10.4236/msa.2013.42013.
[10] M. Syvertsen, B. Ryningen, M. Di Sabatino, W. Palitzsch, H.J. Moeller, C. Audoin, M. Serasset, D. Pelletier, J.P. Rakotoniaina, J. Dieguesz, A. Souto, J. Denafas, L. Petrenene, M. Pranaitis, V. Cyras, R. Zolubas, A. Ulyashin, Recycling of broken Si based structures and solar celss, in: 32nd Eur. Photovolt. Sol. Energy Conf. Exhib.

Recycl. (2016) 1768–1774, https://doi.org/10.4229/EUPVSEC20162016-5DO.15.5.
[11] K. Máčalová, V. Václavík, T. Dvorský, R. Figmig, J. Charvát, M. Lupták, The use of glass from photovoltaic panels at the end of their life cycle in cement composites, Materials 14 (2021) 6655, https://doi.org/10.3390/ma14216655.
[12] G. Granata, F. Pagnanelli, E. Moscardini, T. Havlik, L. Toro, Recycling of photovoltaic panels by physical operations, Sol. Energy Mater. Sol. Cells 123 (2014) 239–248, https://doi.org/10.1016/J.SOLMAT.2014.01.012.
[13] S. Kang, S. Yoo, J. Lee, B. Boo, H. Ryu, Experimental investigations for recycling of silicon and glass from waste photovoltaic modules, Renew. Energy 47 (2012) 152–159, https://doi.org/10.1016/J.RENENE.2012.04.030.
[14] M.B. Hartenstein, C. Stetson, W. Nemeth, V. LaSalvia, S.P. Harvey, S. Theingi, M. Page, C.-S. Jiang, M.M. Al-Jassim, D.L. Young, S. Agarwal, P. Stradins, Trap-assisted dopant compensation prevents shunting in poly-Si passivating interdigitated back contact silicon solar cells, ACS Appl. Energy Mater. 4 (2021) 10774–10782, https://doi.org/10.1021/acsaem.1c01775.
[15] C. Xiao, D. Yang, X. Yu, P. Wang, P. Chen, D. Que, Effect of dopant compensation on the performance of Czochralski silicon solar cells, Sol. Energy Mater. Sol. Cells 101 (2012) 102–106, https://doi.org/10.1016/j.solmat.2012.02.023.
[16] P. Dias, S. Javimczik, M. Benevit, H. Veit, A.M. Bernardes, Recycling WEEE: extraction and concentration of silver from waste crystalline silicon photovoltaic modules, Waste Manag. 57 (2016) 220–225, https://doi.org/10.1016/j.wasman.2016.03.016.
[17] J. Shin, J. Park, N. Park, A method to recycle silicon wafer from end-of-life photovoltaic module and solar panels by using recycled silicon wafers, Sol. Energy Mater. Sol. Cells 162 (2017) 1–6, https://doi.org/10.1016/j.solmat.2016.12.038.
[18] S. Yousef, M. Tatariants, J. Denafas, V. Makarevicius, S.-I. Lukošiūtė, J. Kruopienė, Sustainable industrial technology for recovery of Al nanocrystals, Si micro-particles and Ag from solar cell wafer production waste, Sol. Energy Mater. Sol. Cells 191 (2019) 493–501, https://doi.org/10.1016/j.solmat.2018.12.008.
[19] W. Palitzsch, U. Loser, A new and intelligent de-metalization step of broken silicon cells and silicon cell production waste in the recycling procedure of crystalline si modules, in: 2011 37th IEEE Photovolt. Spec. Conf., IEEE, 2011, pp. 3269–3270, https://doi.org/10.1109/PVSC.2011.6186635.
[20] Y.K. Yi, H.S. Kim, T. Tran, S.K. Hong, M.J. Kim, Recovering valuable metals from recycled photovoltaic modules, J. Air Waste Manage. Assoc. 64 (2014) 797–807, https://doi.org/10.1080/10962247.2014.891540.
[21] B. Jung, J. Park, D. Seo, N. Park, Sustainable system for raw-metal recovery from crystalline silicon solar panels: from noble-metal extraction to lead removal, ACS Sustain. Chem. Eng. 4 (2016) 4079–4083, https://doi.org/10.1021/acssuschemeng.6b00894.
[22] C. Zhang, Q. Ma, M. Cai, Z. Zhao, H. Xie, Z. Ning, D. Wang, H. Yin, Recovery of porous silicon from waste crystalline silicon solar panels for high-performance lithium-ion battery anodes, Waste Manag. 135 (2021) 182–189, https://doi.org/10.1016/j.wasman.2021.08.037.
[23] N. Yuge, K. Hanazawa, K. Nishikawa, H. Terashima, Removal of phosphorus, aluminum and Calcium by evaporation in molten silicon, J. Jpn. Inst. Metals 61 (1997) 1086–1093.
[24] N. Yuge, M. Abe, K. Hanazawa, H. Baba, N. Nakamura, Y. Kato, Y. Sakaguchi, S. Hiwasa, F. Aratani, Purification of metallurgical-grade silicon up to solar grade, Prog. Photovoltaics Res. Appl. 9 (2001) 203–209, https://doi.org/10.1002/pip.372.
[25] T. Miki, K. Morita, N. Sano, Thermodynamics of phosphorus in molten silicon, Metall. Mater. Trans. B 27 (1996) 937–941.
[26] A. Hoseinpur, J. Safarian, Phosphorus removal from Al-doped silicon by vacuum refining, in: 35th Eur. Photovolt. Sol. Energy Conf. Exhib. Phosphorus, 2018, pp. 469–472, https://doi.org/10.4229/35thEUPVSEC20182018. Bruxel.
[27] J. Safarian, M. Tangstad, Vacuum refining of molten silicon, Metall. Mater. Trans. B 43 (2012) 1427–1445, https://doi.org/10.1007/s11663-012-9728-1.
[28] E.S. Marstein, The Research Center for Sustainable Solar Cell Technology, 2019. Oslo, https://susoltech.no/files/2020/05/FME-SULSOLTECH-Annual-Report-2019.pdf. (Accessed 24 May 2022). accessed.
[29] A. Hoseinpur, J. Safarian, Vacuum refining of silicon at ultra-high temperatures, Vacuum 184 (2021), 109924, https://doi.org/10.1016/j.vacuum.2020.109924.
[30] A. Hoseinpur, J. Safarian, Mechanisms of graphite crucible degradation in contact with Si–Al melts at high temperatures and vacuum conditions, Vacuum 171 (2020), 108993, https://doi.org/10.1016/j.vacuum.2019.108993.
[31] A. Hoseinpur, S. Andersson, K. Tang, J. Safarian, Selective vacuum evaporation by the control of the chemistry of gas phase in vacuum refining of Si, Langmuir 37 (2021) 7473–7485, https://doi.org/10.1021/acs.langmuir.1c00876.
[32] A. Hoseinpur, K. Tang, J. Safarian, Kinetic study of vacuum evaporation of elements from ternary melts; case of dilute solution of P in Si-Al melts, Separ. Purif. Technol. 235 (2020), 116284, https://doi.org/10.1016/j.seppur.2019.116284.
[33] J. Safarian, K. Tang, K. Hildal, Vacuum Treatment of Ferrosilicon, in: 2015 Sustain. Ind. Process. Summit, 2015, pp. 261–268. http://www.flogen.org/sips2015/paper-3-69.html.
[34] J. Safarian, M. Tangstad, Kinetics and mechanism of phosphorus removal from silicon in vacuum induction refining, High Temp. Mater. Process. 31 (2012) 73–81, https://doi.org/10.1515/htmp.2011.143.
[35] A. Ciftja, T.A. Engh, M. Tangstad, Wetting properties of molten silicon with graphite materials, Metall. Mater. Trans. 41 (2010) 3183–3195, https://doi.org/10.1007/s11661-010-0362-8.
[36] A. Ciftja, M. Tangstad, T.A. Engh, Wettability of Silicon with Refractory Materials : A Review, 2008.
[37] E.L. Bjørnstad, G. Tranell, Nucleation of SiO 2 -CaO-Al 2 O 3 slag in oxidative ladle refining of metallurgical grade silicon, Metall. Mater. Trans. B Process Metall. Mater. Process. Sci. 52 (2021) 1392–1412, https://doi.org/10.1007/S11663-021-02132-7/FIGURES/22.
[38] E.L. Bjørnstad, I.H. Jung, M.A. Van Ende, G. Tranell, Oxidative refining of metallurgical grade silicon: lab-scale measurements on the overarching refining behavior of Ca and Al, Metall. Mater. Trans. B Process Metall. Mater. Process. Sci. 53 (2022) 1103–1111, https://doi.org/10.1007/S11663-022-02425-5/FIGURES/10.
[39] FactSage version8. 1 (2022). www.factsage.com.
[40] A. Hoseinpur, D. Sergeev, J. Safarian, On the Phosphorus Evaporation from Liquid Silicon by Knudsen Effusion Mass Spectrometry, Metall. Mater. Trans. B (n.d.). https://doi.org/10.1007/s11663-022-02445-1..
[41] A. Schei, J.K. Tuset, H. Tveit, Production of high silicon alloys, chapter 13, Tapir forlag, Trondheim, 1998, p. 292.
[42] S. Pizzini, Towards solar grade silicon: challenges and benefits for low cost photovoltaics, Sol. Energy Mater. Sol. Cells 94 (2010) 1528–1533, https://doi.org/10.1016/j.solmat.2010.01.016.
[43] A. Hoseinpur, S. Andersson, M. Müller, K. Tang, J. Safarian, Boron removal from silicon melt by gas blowing technique, High Temp. Mater. Process. 41 (2022) 69–91, https://doi.org/10.1515/htmp-2022-0011.
[44] A. Hoseinpur, G. Tranell, J. Safarian, Phosphorus and Boron removal from Si by vacuum and gas refining, Silcion Chem. Sol. Ind. XV (2020) 261–272.
[45] A. Cuevas, M. Forster, F. Rougieux, D. Macdonald, Compensation engineering for silicon solar cells, Energy Proc. 15 (2012) 67–77, https://doi.org/10.1016/j.egypro.2012.02.008.